Extraordinary thermoelectric performance, thermal stability and mechanical properties of n-type $Mg_3Sb_{1.5}Bi_{0.5}$ through multi-dopants at interstitial site

Feng Jiang[1,2], Tao Feng[1], Yongbin Zhu[1], Zhijia Han[1], Rui Shu[1], Chen Chen[2], Yiwen Zhang[1], Chengliang Xia[2], Xinzhi Wu[1], Hulei Yu[2], Chengyan Liu[1], Yue Chen[2*] and Weishu Liu[1,3*]

Affiliations

[1]Department of Materials Science and Engineering, Southern University of Science and Technology, Shenzhen 518055, Guangdong, China

[2]Department of Mechanical Engineering, The University of Hong Kong, Pokfulam Road, Hong Kong SAR, China

[3]Guangdong Provincial Key Laboratory of Functional Oxide Materials and Devices, Southern University of Science and Technology, Shenzhen 518055, Guangdong, China

Authors to whom correspondence should be addressed: liuws@sustech.edu.cn (Weishu Liu), yuechen@hku.hk (Yue Chen)

Abstract

Mg_3Sb_2-based thermoelectric materials have attracted much interest since the discovery of their excellent n-type thermoelectric performance with excess Mg content and proper dopant. Herein, we proposed a doping diagram for Mg_3Sb_2-based material in a binary parameters space of electronegativity difference and atomic radius difference of extrinsic elements with Mg atom. Based on this doping diagram, we designed a multiple interstitial doped TM_x:$Mg_3Sb_{1.5}Bi_{0.5}$ (TM = $Cr_{1/5}Mn_{1/5}Fe_{1/5}Co_{1/5}Cu_{1/5}$) material, and achieved a high dimensionless figure of merit value of 0.76 at room temperature and 1.83 at 500 °C, respectively. The multiple interstitial dopants significantly suppress the formation of Mg vacancy, which is of great importance in protecting the electrical transport channel and improving the thermal stability. Besides, the mechanical properties are also enhanced due to the random distribution of elements in the matrix, impeding the migration of dislocations. Our work verifies the benefits of maximized sub-lattice disordering through the multi-elements doping strategy in the $Mg_3Sb_{1.5}Bi_{0.5}$ material.

Keywords: Doping diagram; Mg_3Sb_2-based; thermoelectric; electronegativity; multiple dopants

1. Introduction

The thermoelectric device has attracted considerable interest for its ability to generate electricity from a temperature gradient (TEG) and to realize active cooling with an external electrical current (TEC) [1]. The efficiency of a TEG or TEC device is strongly relative to the performance of thermoelectric materials, which is expressed by the dimensionless figure of merit, $ZT = S^2\sigma T/\kappa$, where S, σ, κ and T, are the Seebeck coefficient, the electrical conductivity, the thermal conductivity, and the absolute temperature, respectively [2]. However, these transport parameters are strongly coupled, resulting in a challenge in raising the ZT value [3, 4]. External doping is necessary to optimize the carrier concentration or adjust the R-space microstructure and K-space band-edge structure for a high ZT [5-7].

Recently, maximizing the disordering of sub-lattice has been considered to be important in manipulating the transport of electrons and phonons through multiple dopants. The progress from single fillers to double fillers and triple fillers manifested one of the benefits, scattering broad-frequency phonons [8]. Such a multiple filler strategy was widely investigated in both n-type and p-type filled-Skutterudites [9, 10]. Similar multiple dopants at a sub-lattice scattering phonon was also reported in the (Ti/Zr/Hf)CoSb [11], Mg_2(Si/Ge/Sn) [12], Cu_2(Te/Se/S) [13], (Sn/Mn/Ge/Pb)Te [14, 15], Co(Sb/Te/Sn)$_3$ [16]. Furthermore, the disordering sub-lattice with multiple elements has a high configurational entropy, providing a thermodynamic drive force to push the materials transition from the low symmetry structure into high symmetry one, which is favored to have a high power factor [13, 17]. Besides, it is believed that the construction of high entropy at the cation-site of Bi_2Se_3 stabilize the compound and suppressed the Se vacancy, and then reaches a p-type thermoelectric material $Bi_{0.8}Sb_{0.8}In_{0.4}Se_3$ [18]. The increased entropy is also a fruitful dimension to guide the design of new thermoelectric materials [19]. However, the selection of multiple elements for a given sub-lattice is still mainly limited by the congener elements.

Mg_3Sb_2-based materials have attracted much interest due to their excellent n-type thermoelectric performance [20, 21], especially near room temperatures [22, 23]. The past few years have witnessed extensive doping investigations, including elements Te, Se, and S in the Sb sublattice [21, 24, 25]; Sc, Y, and Gd in the Mg-sublattice [26-28]; Mn, and Mg in the interstitial site [22, 29, 30] respectively. Nevertheless, to the best of our knowledge, the effect of multiple dopants on the

Mg_3Sb_2-based materials is still lack in investigation. We want to construct a doping diagram for the Mg_3Sb_2-based materials in this work.

Herein, we aim to investigate the effect of multiple dopants at the interstitial site on the properties of $Mg_3Sb_{1.5}Bi_{0.5}$ system since the interstitial site doping has less limit in the valence charge as compared with cation-sublattice and anion-sublattice. Firstly, we calculate the formation energy to search for the possible dopant at the interstitial site from the family of transition metals. Secondly, a doping diagram is constructed with electronegativity difference and atomic radius difference between transition metals and Mg atom. Thirdly, we choose the multiple interstitial dopant combination, i.e. Cr, Mn, Fe, Co, and Cu, and investigate the thermoelectric transport properties, the thermal stability, and mechanical properties of $Mg_3Sb_{1.5}Bi_{0.5}$. Our work provides an intuitive insight into selecting proper dopants on the Mg_3Sb_2-based materials, verifying the strategy to achieve high thermoelectric performance through multiple interstitial doping approaches.

2. Methods

2.1 Sample preparation

Raw materials Mg (turnings, 99.9%), Sb (shots, 99.99%), Bi (shots, 99.99%), Te (shots, 99.999%), and transition metals with high purity (>99.8%) were weighed according to the nominal composition of $TM_xMg_{3.2}Sb_{1.5}Bi_{0.49}Te_{0.01}$ (TM = $Cr_{1/5}Mn_{1/5}Fe_{1/5}Co_{1/5}Cu_{1/5}$, x = 0, 0.002, 0.01, 0.02) in a glove box with both oxygen and water level less than 1 ppm. Hereafter, we refer to the as-fabricated samples as TM_x:$Mg_3Sb_{1.5}Bi_{0.5}$. The starting materials were ball milled for 8 h with a SPEX 8000D and then sintered at 825 ℃ for 5 min with a pressure of 50 MPa in a spark plasma sintering machine (SPS, 211LTX; Fuji, Co, Ltd.). The as-fabricated polycrystal bulks have a diameter of 12.7 mm and a height of ~7 mm, which is large enough for measuring the electrical and thermal properties in the direction perpendicular to the pressure direction. The thermal stability of pristine and $TM_{0.01}Mg_3Sb_{1.5}Bi_{0.5}$ material was performed by the annealing treatment at 400 ℃ for different annealing days under a high vacuum level of less than 1×10^{-2} Pa in quartz tubes.

2.2 Characterizations

The crystalline structures of the as-fabricated TM_x:$Mg_3Sb_{1.5}Bi_{0.5}$ bulks were characterized by X-ray diffraction (XRD, Rigaku SmartLab) using Cu K_α radiation (λ =1.54Å) operating at 45 kV, 200 mA. The elemental compositions for different doped $Mg_3Sb_{1.5}Bi_{0.5}$ materials after annealing treatment are analyzed through the energy-dispersive X-ray spectroscopy (EDS) mapping performed on field-emission scanning electron microscopy (FESEM). For each sample, we

measured three different areas to calculate the average composition. Then we further analyze four local regions in each area. Thus, an average value of 12 EDS mapping results is adapted for each sample.

2.3 Thermoelectric transport properties measurement

Electrical resistivity and Seebeck coefficient of the as-fabricated TM_x:$Mg_3Sb_{1.5}Bi_{0.5}$ bulks were measured simultaneously with a ZEM-3 (ZEM3; ULVAC Riko) in a helium atmosphere from room temperature to 500 ℃. Thermal conductivity was determined by the equation $\kappa = C_p \times D \times d$, where the specific heat capacity C_p was measured by differential scanning calorimeter (DSC, Netzsch), thermal diffusivity D was measured by the laser flash method (LFA 467; Netzsch), and density d was calculated by the Archimedean method. The Hall coefficients (R_H) for the as-fabricated TM_x:$Mg_3Sb_{1.5}Bi_{0.5}$ bulks were measured using Physical Property Measurement Systems (PPMS-14L, Quantum Design) under a reversible magnetic field of 2 T. The Hall carrier concentration and the carrier mobility are calculated by $p_H = 1/|R_H|e$, and $\mu_H = |R_H|/\rho$, receptivity, where e is the electron charge and ρ is the measured electrical resistivity from ZEM-3.

2.4 Mechanical properties measurement

Nanoindentation tests were performed on the Nano Indenter G200 (KLA-Tencor, America) with a maximum load of 200 mN. Young's modulus and hardness can be obtained through the commercial software calculation based on the measured curves. Compression tests were carried out on a universal testing machine (INSTRON) with a displacement speed of 0.25 mm min^{-1} at room temperature and 200 ℃. The testing samples are cut into a cylinder with a diameter of 4.00 mm and a height of ~6.50 mm from an ingot obtained in SPS.

2.5 Defect formation energy calculations

First-principle calculations were carried out on the basis of density functional theory using the projector augmented wave method, as implemented in the Vienna ab-initio Simulation Package (VASP) [31], and the Perdew-Burke-Ernzerhof generalized gradient approximation (PBE-GGA) was applied with a plane wave cutoff energy of 550 eV [32]. The defect formation energies of the periodic table element doped Mg_3Sb_2 were carried out on a supercell ($3 \times 3 \times 2$ primitive cell) with an external dopant on the five potential doping sites, i.e. Mg1 site (0, 0, 0), Mg2 site (1/3, 2/3, 0.368), Sb site (2/3, 1/3, 0.225), the interstitial site (1/3, 2/3, 0.072), and the cage site (0, 0, 0.5). A $3 \times 3 \times 3$ Monkhorst-Pack k-point mesh [33] was used for supercell energy calculations. The atomic positions were fully relaxed until the forces on each atom were less than 0.01 eV/Å, and total energy differences between two consecutive steps were less than 10^{-6} eV. We used $3s^2$, $5s^25p^3$, and

$6s^26p^3$ for the valence electronic configurations of Mg, Sb, and Bi in the pseudopotentials, respectively.

The preferred doping site for periodic table elements in the Mg_3Sb_2-based materials was determined by the calculation of defect formation energy, according to the Eq. 1 [34, 35]:

$$E^f = E_{tot} - E_{pri} - E_r + E_x \quad (1)$$

where E_{tot} and E_{pri} represent the energies of a defect-contain and perfect supercell, respectively. E_r and E_x are the elemental energy of the substituted atom and doping atom in their pure substance, respectively. In this work, we mainly focus on the defect formation energies in the neutral state, and the effect of the charge state resulting from doping atom may be concerned for precise calculations in the future work.

3. Results and discussions

3.1 Doping diagram of Mg_3Sb_2-based thermoelectrics

Fig. 1 (a) shows the defect formation energies of different 20 dopants, including, Ca, Sc, Y, Ti, Hf, Nb, Mo, Cr, Mn, Fe, Co, Ni, Cu, Ag, Zn, Al, Ga, Ge, Bi, and Te in their five potential doped sites of Mg_3Sb_2, i.e. Mg1 site (0, 0, 0), Mg2 site (1/3, 2/3, 0.368), Sb site (2/3, 1/3, 0.225), the interstitial site (i1) (1/3, 2/3, 0.072), and the cage site (i2) (0, 0, 0.5) (**Fig. 1(b)**). Mg_3Sb_2 crystalizes in an inverse α-La_2O_3 structure-type (Space group $P\bar{3}m1$) with an Mg^{2+} layer and $[Mg_2Sb_2]^{2-}$ skeleton stacked in the ABAB sequence along the *c* axis direction [36, 37]. Based on the defect formation energy, the cage site was firstly excluded for all the investigated dopants showing the highest formation energy as compared with other sub-lattice sites. In the following part, we will discuss the favorable dopants in the sublattice site in the sequence of Mg1 site, the interstitial site, Mg2 site, and Sb site for elemental occupation.

Firstly, Ca, Sc, Y, Ti, Hf and Nb prefer to occupy the Mg1 as shown in the green region of **Fig. 1 (a)**. Ca belongs to alkali element, which is consistent with the definition of A site for an AB_2X_2-type Zintl compound [38]. Besides, Sc and Y were reported as effective electron providers for Mg_3Sb_2-based materials both in theoretical calculations [39, 40] and experiments [23, 26, 41]. While for Hf and Nb, Ren *et al*. have suggested these two elements could tune the scattering mechanism as they substitute the Mg1 atom [42, 43]. Secondly, the cyan region of **Fig. 1 (a)** indicates that the lowest formation energy site for transition metals Mo, Cr, Mn, Fe, Co, Ni, Cu, and Ag is the interstitial site. Mn and Cu have been reported to occupy the interstitial site and have made great

advances in thermoelectric performance [22, 44]. While for Fe, Co, Ni, and Ag, Ren *et al*. suggested that they might prefer the Mg1 site according to their experimental work [43, 45]. However, our calculations sugget the interstitial site is more energetically favorable for these transition metals. Thirdly, Zn, Ga, and Al prefer to replace Mg2 atom according to our calculations, the yellow region of **Fig. 1 (a)**. Zn has d^{10} electron orbits and prefers to occupy Mg2 site [46]. Besides, Al has the lowest defect formation energy of the Mg2 site, which is consistent with reported experiment results [47]. Finally, Ge, Bi, and Te tend to occupy the Sb site in the pink region of **Fig. 1 (a)**. Bi has been applied to tune the band structure of Mg_3Sb_2 and reduce the thermal conductivity [48, 49], while Te is an effective dopant that provides extra electrons in the system. Beside, Recently reported Ge dopant can significantly decrease the thermal conductivity when occupied at Sb site [50]. Among those elements, Ti, Mo, Cr, and Ga have not yet been investigated.

Based on the above analyses, we suggest that there is a general rule to intuitively present the preferred doping site of Mg_3Sb_2 for the periodic table elements instead of the defect formation energy calculations. Generally, the electronegativity and atomic radius of constituted elements are key parameters to affect the crystal structure, the hardness, and the carrier concentration of host materials [51-53]. Therefore, we try to construct a doping diagram based on the electronegativity difference and atomic radius difference between the doping element and Mg element as shown in **Fig. 1 (c)**. To be addressed, the Allred-Rochow electronegativity [54] and atomic radius [55] of periodic table elements are utilized in this work and detailed data are presented in the supporting information (**Table S1**). Four regions were clearly separated. Our theoretical calculations (Blue circles) exhibit high consistency with reported defect formation energies (Brown triangles) [40, 56, 57]. In addition, we also summarized various reported Mg_3Sb_2-based thermoelectrics with different dopants in this doping diagram (Red stars) [22, 25, 26, 28, 42, 43, 58-69]. It is shown that the located regions for reported doped elements are coincided with their occupied sites in experiments, indicating the high effectiveness of this doping diagram in guiding the preferred doping sites of extrinsic dopants on Mg_3Sb_2-based materials.

In our previous work, we have suggested that the interstitial site doping has a less detrimental impact on the band edge of Mg_3Sb_2 material [70], and could significantly suppress the formation of Mg vacancy [22, 71]. Herein, we would like to further investigate the effect of multiple interstitial dopants on the thermoelectric properties of Mg_3Sb_2-based materials. The X-ray diffraction (XRD) patterns of $TM_xMg_{3.2}Sb_{1.5}Bi_{0.49}Te_{0.01}$ (TM = CrMnFeCoCu, x = 0, 0.002, 0.01, 0.02) are presented in **Fig. S1**. All the diffraction peaks are well indexed with reported inverse α-La_2O_3 structure-type (Mg_3Sb_2, PDF#65-3458) and no obvious impurity peaks are observed, indicating the substantial solubility of these transition metals in $Mg_3Sb_{1.5}Bi_{0.5}$ system. Additionally, EDS mapping results

shown in Fig. S2 reveal the uniform doping in the as-fabricated $TM_{0.01}Mg_{3.2}Sb_{1.5}Bi_{0.5}$.

3.2 Multiple-elements Doped Mg_3Sb_2

Fig. 2 shows the electrical transport properties of as-fabricated TM_x:$Mg_3Sb_{1.5}Bi_{0.5}$ (x = 0, 0.002, 0.01, 0.02) materials. The room temperature electrical resistivity of TM_x:$Mg_3Sb_{1.5}Bi_{0.5}$ bulks continuously decrease from 18.3 to 15.0, 13.8, and 13.2 μΩm as TM content increases from x = 0 to 0.002, 0.01, and 0.02, respectively (**Fig. 2 (a)**). The Seebeck coefficients of all as-fabricated TM_x:$Mg_3Sb_{1.5}Bi_{0.5}$ bulks exhibit a degenerate behavior, showing a near-linear variation with temperature from -200 μV K^{-1} to -300μV K^{-1} and a weak correction with TM doping content (**Fig. 2 (b)**). Owing to significant decrease in electrical resistivity from x = 0 to x = 0.2, the power factor therefore increases 17% at room temperature from 2386 μW m^{-1} K^{-2} (x = 0) to 2799 μW m^{-1} K^{-2} (x = 0.02), and 20% at 500 ℃ from 1572 μW m^{-1} K^{-2} (x = 0) to 1821 μW m^{-1} K^{-2} (x = 0.01) (**Fig. 2 (c)**). The high power factor is critical for the power generation application [72]. According to the relationship of $1/\rho = n_H e \mu_H$, the decreased electrical resistivity could be resulted from both the carrier concentration (n_H) and carrier mobility (μ_H). The Hall measurement shows that the carrier concentration increases by 7% from 2.8×10^{19} to 3.0×10^{19} cm^{-3} while carrier mobility increases by 29% from 124 to 160 cm^2 V^{-1} s^{-1} as TM doping content increases from x = 0 to x = 0.02 (**Table 1**). The slightly increased carrier concentration suggests the interstitial dopants behave as weak donors. Similar donor behavior has been widely verified in the filled Skutterudites [8, 73] and Cu interstitial-doped $Bi_2Te_{2.7}Se_{0.3}$ [74]. Furthermore, the increased carrier mobility might be related to the decreased scattering from the defects. In our previous work, we have suggested that the interstitial Mn dopant could significantly suppress the formation of Mg vacancy [22, 71], which is consistent with the increased Mg content per formula with the multiple TM interstitial dopants (**Fig. S7**). Additionally, Mao *et al*. suggested that carriers were subject less to scattering by Mg vacancy [75]. Moreover, the grain size of $TM_{0.01}Mg_3Sb_{1.5}Bi_{0.5}$ sample is comparable with that of the undoped sample (**Fig. S3**). Therefore, the electrical transport channel can be well protected by the further suppression of Mg vacancy through multiple TM dopants, leading to a further increase of carrier mobility. **Fig. 2 (d)** compares the weighted mobility $U = \mu(m^*/m_0)^{3/2}$ (where μ is the Hall carrier mobility and m* is the effective mass) of the as-fabricated TM_x:$Mg_3Sb_{1.5}Bi_{0.5}$ bulks with previous reported transition-metal doped $Mg_3Sb_{1.5}Bi_{0.5}$ [43, 44, 60, 61] as well as $Mg_3Sb_{2-x}Bi_x$ materials [26, 27, 71]. The effective mass of the as-fabricated TM_x:$Mg_3Sb_{1.5}Bi_{0.5}$ bulks is 1.5 m_0 (**Fig. S4**), which is comparable with previously reported $Mg_3Sb_{1.5}Bi_{0.5}$ bulks with co-dopants of Mn and Te [60], and Fe and Te [43]. Therefore, the increased carrier mobility of the as-fabricated $TM_{0.01}Mg_3Sb_{1.5}Bi_{0.5}$ sample contributes much to the higher U value of 293.9 cm^2 V^{-1} s^{-1} among the reported $Mg_3Sb_{2-x}Bi_x$ family. The high weighted mobility is consistent with the observed high power factor.

Fig. 3 shows the thermal transport properties and dimensionless figure of merit for the as-fabricated TM_x:$Mg_3Sb_{1.5}Bi_{0.5}$ (x = 0, 0.002, 0.01, 0.02). As shown in **Fig. 3 (a)**, all the samples show a continuous decrease in the whole temperature range of room temperature to 500 ℃, indicating no obvious bipolar effect. The total thermal conductivity near room temperatures of the as-fabricated $TM_xMg_3Sb_{1.5}Bi_{0.5}$ bulks is slightly higher than the TM-free sample due to the increased electrical thermal conductivity. Based on the Wiedemann-Franz law, we further estimated the lattice thermal conductivity (**Fig. 3 (b)**), which is subtracted by electrical thermal conductivity from total thermal conductivity, i.e. $\kappa_{lat} = \kappa_{tot} - LT/\rho$, where ρ is the measured electrical resistivity, L is Lorenz number calculated based on the single parabolic model with acoustic phonons scattering. The relationship between Lorenz number, Seebeck coefficient, and Fermi level is expressed as follows [74]:

$$S = \pm \frac{k_B}{e}\left[\frac{(r+5/2)F_{r+3/2}(\eta)}{(r+3/2)F_{r+1/2}(\eta)} - \eta\right] \quad 1)$$

$$L = \frac{{k_B}^2}{e^2}\left[\frac{(r+7/2)F_{r+5/2}(\eta)}{(r+3/2)F_{r+1/2}(\eta)} - \left[\frac{(r+5/2)F_{r+3/2}(\eta)}{(r+3/2)F_{r+1/2}(\eta)}\right]^2\right] \quad 2)$$

$$F_n(\eta) = \int_0^\infty \frac{\xi^n}{\exp(\xi-\eta)+1} d\xi \quad 3)$$

where k_B, e, r, η, F_n, and ξ are the Boltzmann constant, electron charge, scattering parameter, reduced Fermi level, nth Fermi-Dirac integral, and reduced energy, respectively. As shown in Fig. 3 (b), the κ_L firstly decreases as x increases from 0 to 0.01 and then increases as x = 0.02. Specifically, the κ_L of as-fabricated TM_x:$Mg_3Sb_{1.5}Bi_{0.5}$ decreases 5% at room temperature from 0.78 W m^{-1} K^{-1} (x = 0) to 0.74 W m^{-1} K^{-1} (x = 0.01), and 9% at 500 ℃ 0.57 W m^{-1} K^{-1} (x = 0) to 0.52 W m^{-1} K^{-1} (x = 0.01). While, considering the lattice thermal conductivity, the interstitial TM elements are weak phonon scattering in the as-fabricated TM_x:$Mg_3Sb_{1.5}Bi_{0.5}$. The phonon scattering by the interstitial dopants could be counteracted by the reduction of Mg-vacancy defects to the phonon scattering as compared with other reported interstitial dopants, such as Cu in $Bi_2Te_{2.7}Se_{0.3}$ [74], and Mn in $Mg_3Sb_{1.5}Bi_{0.5}$ [22, 76], which were also reported the obvious phonon scattering. **Fig. 3 (c)** shows the temperature-dependent ZT values of the as-fabricated TM_x:$Mg_3Sb_{1.5}Bi_{0.5}$. Owing to the optimized power factor and the decreased lattice thermal conductivity, the ZT values increases by 12% at room temperature from 0.68 (x = 0) to 0.76 (x = 0.01), and 18% at 500 ℃ from 1.55 (x = 0) to 1.83 (x = 0.01). **Fig. 3 (d)** compares the room temperature ZT and ZT_{avg} in the range of 50 – 250 ℃ of the as-fabricated $TM_{0.01}Mg_3Sb_{1.5}Bi_{0.5}$ sample with other reported $Mg_3Sb_{1.5}Bi_{0.5}$ materials [26, 43, 44, 60, 71] and a classic n-type nano-Bi_2Te_3 material [74]. It shows that the as-fabricated $TM_{0.01}Mg_3Sb_{1.5}Bi_{0.5}$ sample has a higher room temperature ZT value of 0.76 among $Mg_3Sb_{1.5}B_{i0.5}$ family, and is comparable to

0.90 for the classic Bi_2Te_3 materials. Besides, the as-fabricated $TM_{0.01}Mg_3Sb_{1.5}Bi_{0.5}$ sample possesses a high ZT_{avg} of 1.17 in the temperature range from 50 ℃ to 250 ℃, which is higher than that of previous reported transition-doped Mg_3Sb_2-based materials and reported Bi_2Te_3 materials, suggesting that multiple TM dopants can effectively improve the overall TE performance and enable the Mg_3Sb_2 as a candidate in practical application at room and mid-temperature.

3.3 Thermal stability

Thermal stability is a crucial indicator to justify the reliability of the long-term services of thermoelectric materials at high temperatures [74, 77]. Therefore, annealing treatment at 400 ℃ for 0 day, 3 days, 7 days and 10 days were conducted. **Fig. 4** compares the electrical properties of the as-fabricated $TM_{0.01}Mg_3Sb_{1.5}Bi_{0.5}$ sample with the TM-free $Mg_3Sb_{1.5}Bi_{0.5}$ sample after annealing. Firstly, the electrical resistivity of all the samples slightly increased after annealing treatment (**Fig. 4 (a,b)**), which is due to the strong deterioration of carrier mobility (**Fig. S5**). Secondly, for the Seebeck coefficients, the TM-free $TM_{0.01}Mg_3Sb_{1.5}Bi_{0.5}$ sample shows an obvious decrease from -208 to -199, -194, and -189 $\mu V\ K^{-1}$, as the annealing time increases from 0 to 3, 7, and 10 days, respectively (**Fig. 4 (d)**). While the Seebeck coefficients of the as-fabricated $TM_{0.01}Mg_3Sb_{1.5}Bi_{0.5}$ sample are less impacted by annealing treatment (**Fig. 4 (e,f)**). The comparison of thermoelectric transport properties between TM doped and TM-free $Mg_3Sb_{1.5}Bi_{0.5}$ clearly suggests that the TM doping significantly increases thermal stability. The thermally unstable issue in $Mg_3Sb_{1.5}Bi_{0.5}$ thermoelectric materials was known for the Mg evaporation at high temperatures. Some efforts to prevent the Mg loss have been verified as an effective approach, including Mg-vaporing treatment [78] and BN-coating [79]. In our case, the increased thermal stability has resulted from two facts. First, the local bonding between the interstitial dopants and Mg atom could raise the formation energy of Mg vacancy. Second, the multiple dopants of $Cr_{1/5}Mn_{1/5}Fe_{1/5}Co_{1/5}Cu_{1/5}$ increase the entropy of the materials, providing another thermodynamic reason for the improved thermal stability. Additionally, the results of crystal structure, EDS mapping and Hall measurements of $TM_{0.01}Mg_3Sb_{1.5}Bi_{0.5}$ and TM-free $Mg_3Sb_{1.5}Bi_{0.5}$ sample (**Fig. S5 – S7**) further demonstrate the improved thermal stability through multiple interstitial dopants. Consequently, the room temperature power factor of the as-fabricated $TM_{0.01}Mg_3Sb_{1.5}Bi_{0.5}$ sample decreases by 12.6% after annealing treatment for 10 days, which is much less than that (31.3%) of the TM-free $Mg_3Sb_{1.5}Bi_{0.5}$ sample (**Fig. 4 (i)**). The apparent difference in power factor manifests the benefits of multiple interstitial dopants.

Furthermore, **Fig. 5** compares the long-term in-situ electrical properties measurement of the as-fabricated $TM_{0.01}Mg_3Sb_{1.5}Bi_{0.5}$ sample with reported pristine and BN-coated $Mg_{3.2}Sb_{1.5}Bi_{0.5}$ at

400 ℃ [79]. The electrical conductivity of the as-fabricated $TM_{0.01}Mg_3Sb_{1.5}Bi_{0.5}$ sample shows a slight derivation within 3% at 400 ℃ in 65 h, which is much lower than the reported $Mg_{3.2}Sb_{1.5}Bi_{0.49}Te_{0.01}$ sample (20%) and comparable to the BN-coated samples (4%) (**Fig. 5 (a)**). Besides, both Seebeck coefficients and power factor of as-fabricated $TM_{0.01}Mg_3Sb_{1.5}Bi_{0.5}$ sample show less fluctuation than that of reported pristine and BN-coated $Mg_3Sb_{1.5}Bi_{0.5}$ (**Fig. 5 (b,c)**). The well maintained electrical properties of the as-fabricated $TM_{0.01}Mg_3Sb_{1.5}Bi_{0.5}$ sample may be contributed by the stabilization of crystal structure **(Fig. S6**) and significant suppression of Mg vacancy (**Fig. S7**), thus protecting the electrical transport channel (less deterioration to carrier mobility, **Fig. S5**). Besides, we also compared the temperature-dependent thermoelectric properties of initial $TM_{0.01}Mg_3Sb_{1.5}Bi_{0.5}$ sample with the rest sample that was stored in a sample sack at ambient environment after 10 months (**Fig. S9 (a)**). The electrical transport properties near 500 ℃ get about 8 % deterioration after 10 months (Fig. S9), indicating excellent chemical stability of $TM_{0.01}Mg_3Sb_{1.5}Bi_{0.5}$ sample. These results reveal that as-fabricated $TM_{0.01}Mg_3Sb_{1.5}Bi_{0.5}$ material exhibits promising thermal stability, which is owing to the suppression of Mg vacancy, similar to BN coated [79], thus securing the reliability for the operation in TE devices.

3.4 Mechanical properties

Fig. 6 (a) shows the measured nano-indentation curves of as-fabricated pristine, $TM_{0.01}Mg_3Sb_{1.5}Bi_{0.5}$ materials under a maximum load of 200 mN. The Young's modulus estimated through the nano-indentation tests gets an increase from 36.58 GPa for pristine $Mg_3Sb_{1.5}Bi_{0.5}$ to 42.2 GPa for $TM_{0.01}Mg_3Sb_{1.5}Bi_{0.5}$, close to that of our previous reported value [22]. Additionally, the hardness shows the same trend as Young's modulus (**Fig. 6 (c)**). The hardness of as-fabricated $TM_{0.01}Mg_3Sb_{1.5}Bi_{0.5}$ sample is 1.29 GPa, which is better than that of promising thermoelectric materials, such as Bi_2Te_3 (1.14 GPa) [80], $Cu_{1.8}S$-$Ru_{0.01}$ (1.01 GPa) [81], and Nd-doped $Mg_3Sb_{1.5}Bi_{0.5}$ (1.11 GPa) [82]. The multiple dopants at the interstitial site may strengthen the chemical bonding between adjacent layers (**Fig. 6 (b)**), a similar strengthening effect was also observed in MgB_2 doped in GeTe matrix [83].

Fig. 6 (c) shows the compressive stress-strain tests for pristine and $TM_{0.01}Mg_3Sb_{1.5}Bi_{0.5}$ at room temperature and 200 ℃. All the $Mg_3Sb_{1.5}Bi_{0.5}$ samples exhibit promising plasticity as the strain can reach above 30%. The compressive strength increases by 20% at room temperature from 298 MPa pristine $Mg_3Sb_{1.5}Bi_{0.5}$ to 359 MPa for $TM_{0.01}Mg_3Sb_{1.5}Bi_{0.5}$, and 16% at 200 ℃ from 232 MPa for pristine $Mg_3Sb_{1.5}Bi_{0.5}$ to 269 MPa for $TM_{0.01}Mg_3Sb_{1.5}Bi_{0.5}$ (**Fig. 6 (c)**). The room temperature compressive strength of the as-fabricated $TM_{0.01}Mg_3Sb_{1.5}Bi_{0.5}$ is much higher than other state-of-the-art thermoelectrics $Ge_{0.9}Sb_{0.1}Te$ [83], Bi_2Te_3 [84], Cu_2Se [85], SnSe [86], $Cu_{1.9}Ag_{0.1}Te_{0.6}Se_{0.2}S_{0.2}$

[13], RE-doped $Mg_3Sb_{1.5}Bi_{0.5}$ [68], and comparable with α-MgAgSb (390 MPa) [87] (**Fig. 6 (d)**). The improved mechanical properties are owing to the multiple dopants randomly distributed into the interstitial site in the $Mg_3Sb_{1.5}Bi_{0.5}$ matrix. These interstitial dopants can significantly suppress the Mg vacancy and strengthen the chemical bonding between adjacent layers. Besides, the lattice distortion induced by multiple interstitial dopants impedes the dislocation migration, thereby increasing the hardness and compressive strength [13, 88].

4. Conclusions

In summary, we have systematically investigated the dopants for the Mg_3Sb_2-based thermoelectric materials, and constructed a doping diagram for the preferred doping site. We have shown that the transition metals prefer to occupy the interstitial tetrahedron site. Furthermore, we investigated the thermoelectric, thermal stability, and mechanical properties of the multiple transition metals (TM = $Cr_{1/5}Mn_{1/5}Fe_{1/5}Co_{1/5}Cu_{1/5}$) co-doped $Mg_3Sb_{1.5}Bi_{0.5}$. The multiple interstitial dopants are critical in suppressing the formation of Mg vacancy, leading to high weighted mobility and thermal stability. Specifically, an ultrahigh power factor of 2799 $\mu W\ m^{-1}\ K^{-2}$ and a high ZT value of 0.76 was achieved in the as-fabricated $TM_{0.01}Mg_3Sb_{1.5}Bi_{0.5}$. Moreover, Young's modulus, the hardness, and the compressive strength of $TM_{0.01}Mg_3Sb_{1.5}Bi_{0.5}$ sample were significantly enhanced as compared with TM-free $Mg_3Sb_{1.5}Bi_{0.5}$ sample. Our work verified the effectiveness of the multiple doping at the interstitial site in the $Mg_3Sb_{1.5}Bi_{0.5}$ thermoelectric materials to have a synergistically enhancement in both thermoelectric performance and mechanical properties.

Data availability

The data that support the findings of this study are available from the corresponding author upon reasonable request.

Credit author statement

Feng Jiang: Investigation, Data curation, Writing-original draft. **Tao Feng:** Revision, Analysis of data. **Yongbin Zhu:** Data curation. **Zhijia Han:** Revision, methodology. **Rui Shu**: Methodology. **Chen Chen:** Data curation. **Yiwen Zhang**: Methodology. **Chengliang Xia:** Investigation, methodology. **Xinzhi Wu:** Methodology. **Hulei Yu:** Revision, Methodology. **Chengyan Liu:** Revision, methodology. **Yue Chen:** Supervision, Editing, Validation, Funding acquisition. **Weishu**

Liu: Concerptualization, Supervision, Editing, Validation, Methodology, Funding acquisition.

Declaration of competing interest

The authors declare that they have no known competing financial interests or personal relationships that could have appeared to influence the work reported in this paper.

Acknowledgements:

This work was supported by the financial aid from the National Natural Science Foundation of China under Grant No. 51872133, and Guangdong Provincial Key Laboratory Program (2021B1212040001), Shenzhen Key Program for Long-Term Academic Support Plan (20200925164021002). WSL acknowledges the support from the Tencent Foundation through the XPLORER PRIZE. The authors also thanks to the computing time supported by the Center for Comuptational Science and Engineering of SUSTech.

References

[1] W. S. Liu, J. Z. Hu, S. M. Zhang, M. J. Deng, C.-G. Han, Y. Liu, New trends, strategies and opportunities in thermoelectric materials: A perspective, Mater. Today Phys. 1 (2017) 50-60.

[2] R. P. Chasmar, R. Stratton, The Thermoelectric Figure of Merit and its Relation to Thermoelectric Generators, J. Electron. Control 7 (1959) 52-72.

[3] W. S. Liu, X. Yan, G. Chen, Z. F. Ren, Recent advances in thermoelectric nanocomposites, Nano Energy 1 (2012) 42-56.

[4] J. He, T. M. Tritt, Advances in thermoelectric materials research: Looking back and moving forward, Science 357 (2017) 1369.

[5] M. S. Dresselhaus, G. Chen, M. Y. Tang, R. G. Yang, H. Lee, D. Z. Wang, Z. F. Ren, J. P. Fleurial, P. Gogna, New Directions for Low-Dimensional Thermoelectric Materials, Adv. Mater. 19 (2007) 1043-1053.

[6] T. J. Zhu, Y. T. Liu, C. G. Fu, J. P. Heremans, J. G. Snyder, X. B. Zhao, Compromise and Synergy in High-Efficiency Thermoelectric Materials, Adv. Mater. 29 (2017) 1605884-1605909.

[7] Z. Liu, W. Gao, F. Guo, W. Cai, Q. Zhang, J. Sui, Challenges for Thermoelectric Power Generation: From a Material Perspective, Mater. Lab 1 (2022) 220003-220014.

[8] X. Shi, J. Yang, J. R. Salvador, M. Chi, J. Y. Cho, H. Wang, S. Bai, J. Yang, W. Zhang, L. Chen, Multiple-filled skutterudites: high thermoelectric figure of merit through separately optimizing electrical and thermal transports, J. Am. Chem. Soc. 133 (2011) 7837-7846.

[9] G. Rogl, P. Rogl, Skutterudites, a most promising group of thermoelectric materials, Curr. Opin. Green Sustainable Chem. 4 (2017) 50-57.

[10] J. S. Dyck, W. Chen, C. Uher, L. D. Chen, X. F. Tang, T. Hirai, Thermoelectric properties of then-type filled skutterudite $Ba_{0.3}Co_4Sb_{12}$ doped with Ni, J. Appl. Phys. 91 (2002) 3698-3705.

[11] S. Chen, K. C. Lukas, W. S. Liu, C. P. Opeil, G. Chen, Z. F. Ren, Effect of Hf Concentration on Thermoelectric Properties of Nanostructured N-Type Half-Heusler Materials $Hf_xZr_{1-x}NiSn_{0.99}Sb_{0.01}$, Adv. Energy Mater. 3 (2013) 1210-1214.

[12] J. Mao, H. S. Kim, J. Shuai, Z. Liu, R. He, U. Saparamadu, F. Tian, W. Liu, Z. Ren, Thermoelectric properties of materials near the band crossing line in Mg_2Sn–Mg_2Ge–Mg_2Si system, Acta Mater. 103 (2016) 633-642.

[13] Z. X. Zhang, K. P. Zhao, H. Y. Chen, Q. Y. Ren, Z. M. Yue, T.-R. Wei, P. F. Qiu, L. D. Chen, X. Shi, Entropy engineering induced exceptional thermoelectric and mechanical performances in $Cu_{2-y}Ag_yTe_{1-2x}S_xSe_x$, Acta Mater. 224 (2022) 117512-117519.

[14] X. Y. Wang, H. H. Yao, Z. W. Zhang, X. F. Li, C. Chen, L. Yin, K. N. Hu, Y. R. Yan, Z. Li, B. Yu, F. Cao, X. J. Liu, X. Lin, Q. Zhang, Enhanced Thermoelectric Performance in High Entropy Alloys $Sn_{0.25}Pb_{0.25}Mn_{0.25}Ge_{0.25}Te$, ACS Appl. Mater. Interfaces 13 (2021) 18638-18647.

[15] B.-C. Qin, Y. Xiao, Y.-M. Zhou, L.-D. Zhao, Thermoelectric transport properties of Pb–Sn–Te–Se system, Rare Met. 37 (2017) 343-350.

[16] W.-S. Liu, B.-P. Zhang, L.-D. Zhao, J.-F. Li, Improvement of Thermoelectric Performance of $CoSb_{3-x}Te_x$ Skutterudite Compounds by Additional Substitution of IVB-Group Elements for Sb, Chem. Mater. 20 (2008) 7526-7531.

[17] Y. T. Qiu, Y. Jin, D. Y. Wang, M. J. Guan, W. K. He, S. Peng, R. H. Liu, X. Gao, L.-D. Zhao, Realizing high thermoelectric performance in GeTe through decreasing the phase transition temperature

via entropy engineering, J. Mater. Chem. A 7 (2019) 26393-26401.
[18] F. Jiang, C. L. Xia, Y. B. Zhu, Z. J. Han, C. Y. Liu, J. T. Xia, Y. Chen, W. S. Liu, Thermoelectric properties of p-type polycrystalline $Bi_{0.8}Sb_{0.8}In_{0.4}Se_3$, Appl. Phys. Lett. 118 (2021) 193903-193907.
[19] N. Dragoe, Entropy driven synthesis of new materials, Mater. Lab 1 (2022) 220001.
[20] H. Tamaki, H. K. Sato, T. Kanno, Isotropic Conduction Network and Defect Chemistry in $Mg_{3+\delta}Sb_2$-Based Layered Zintl Compounds with High Thermoelectric Performance, Adv. Mater. 28 (2016) 10182-10187.
[21] J. W. Zhang, L. R. Song, S. H. Pedersen, H. Yin, L. T. Hung, B. B. Iversen, Discovery of high-performance low-cost n-type Mg_3Sb_2-based thermoelectric materials with multi-valley conduction bands, Nat. Commun. 8 (2017) 13901-13908.
[22] R. Shu, Y. C. Zhou, Q. Wang, Z. J. Han, Y. B. Zhu, Y. Liu, Y. X. Chen, M. Gu, W. Xu, Y. Wang, W. Q. Zhang, L. Huang, W. S. Liu, $Mg_{3+\delta}Sb_xBi_{2-x}$Family: A Promising Substitute for the State-of-the-Art n-Type Thermoelectric Materials near Room Temperature, Adv. Funct. Mater. 29 (2019) 1807235-1807234.
[23] X. M. Shi, C. Sun, X. Y. Zhang, Z. W. Chen, S. Q. Lin, W. Li, Y. Z. Pei, Efficient Sc-Doped $Mg_{3.05-x}Sc_xSbBi$ Thermoelectrics Near Room Temperature, Chem. Mater. 31 (2019) 8987-8994.
[24] J. Mao, Y. X. Wu, S. W. Song, Q. Zhu, J. Shuai, Z. H. Liu, Y. Z. Pei, Z. F. Ren, Defect Engineering for Realizing High Thermoelectric Performance in n-Type Mg_3Sb_2-Based Materials, ACS Energy Lett. 2 (2017) 2245-2250.
[25] J. W. Zhang, L. R. Song, K. A. Borup, M. R. V. Jørgensen, B. B. Iversen, New Insight on Tuning Electrical Transport Properties via Chalcogen Doping in n-type Mg_3Sb_2-Based Thermoelectric Materials, Adv. Energy Mater. 8 (2018) 1702776-1702782.
[26] X. M. Shi, T. T. Zhao, X. Y. Zhang, C. Sun, Z. W. Chen, S. Q. Lin, W. Li, H. Gu, Y. Z. Pei, Extraordinary n-Type Mg_3SbBi Thermoelectrics Enabled by Yttrium Doping, Adv. Mater. 31 (2019) 1903387-1903394.
[27] J. W. Zhang, L. R. Song, B. B. Iversen, Rapid One-Step Synthesis and Compaction of High-Performance n-Type Mg_3Sb_2 Thermoelectrics, Angew. Chem. Int. Ed. Engl. 59 (2020) 4278-4282.
[28] J. D. Lei, H. Wuliji, K. P. Zhao, T.-R. Wei, Q. Xu, P. Li, P. F. Qiu, X. Shi, Efficient lanthanide Gd doping promoting the thermoelectric performance of Mg_3Sb_2-based materials, J. Mater. Chem. A 9 (2021) 25944-25953.
[29] J. Zhang, L. Song, B. B. Iversen, Probing Efficient N-Type Lanthanide Dopants for Mg_3Sb_2 Thermoelectrics, Adv. Sci. 7 (2020) 2002867.
[30] J. W. Yang, G. D. Li, H. T. Zhu, N. Chen, T. B. Lu, J. L. Gao, L. W. Guo, J. S. Xiang, P. J. Sun, Y. Yao, R. G. Yang, H. Z. Zhao, Next-generation thermoelectric cooling modules based on high-performance $Mg_3(Bi,Sb)_2$ material, Joule 6 (2021) 1-12.
[31] G. Kresse, J. Furthmüller, Efficiency of ab-initio total energy calculations for metals and semiconductors using a plane-wave basis set, Comput. Mater. Sci. 6 (1996) 15-50.
[32] P. E. Blochl, Projector augmented-wave method, Phys. Rev. B Condens. Matter. 50 (1994) 17953-17979.
[33] H. J. Monkhorst, J. D. Pack, Special points for Brillouin-zone integrations, Phys. Rev. B 13 (1976) 5188-5192.
[34] K. Matsunaga, T. Tanaka, T. Yamamoto, Y. Ikuhara, First-principles calculations of intrinsic defects in Al_2O_3, Phys. Rev. B 68 (2003) 085110-085118.
[35] C. G. Van de Walle, J. Neugebauer, First-principles calculations for defects and impurities: Applications to III-nitrides, J. Appl. Phys. 95 (2004) 3851-3879.

[36] C. L. Condron, S. M. Kauzlarich, F. Gascoin, G. J. Snyder, Thermoelectric Properties and Microstructure of Mg_3Sb_2, J. Solid State Chem. 179 (2016) 2252-2257.
[37] Z. J. Han, J.-W. Li, F. Jiang, J. T. Xia, B.-P. Zhang, J.-F. Li, W. S. Liu, Room-temperature thermoelectric materials: Challenges and a new paradigm, J. Materiomics (2021) 427-436.
[38] J. Shuai, J. Mao, S. W. Song, Q. Y. Zhang, G. Chen, Z. F. Ren, Recent progress and future challenges on thermoelectric Zintl materials, Mater. Today Phys. 1 (2017) 74-95.
[39] P. Gorai, E. S. Toberer, V. Stevanović, Effective n-type doping of Mg_3Sb_2 with group-3 elements, J. Appl. Phys. 125 (2019) 025105-025110.
[40] C. L. Xia, J. Cui, Y. Chen, Effect of group-3 elements doping on promotion of in-plane Seebeck coefficient of n-type Mg_3Sb_2, J. Materiomics 6 (2020) 274-279.
[41] J. S. Liang, X. L. Shi, Y. Peng, W. D. Liu, H. Q. Yang, C. Y. Liu, J. L. Chen, Q. Zhou, L. Miao, Z. G. Chen, Synergistic Effect of Band and Nanostructure Engineering on the Boosted Thermoelectric Performance of n‐Type $Mg_{3+\delta}(Sb, Bi)_2$ Zintls, Adv. Energy Mater. (2022) 2201086-2201095.
[42] J. Shuai, J. Mao, S. W. Song, Q. Zhu, J. F. Sun, Y. M. Wang, R. He, J. W. Zhou, G. Chen, D. J. Singh, Z. F. Ren, Tuning the carrier scattering mechanism to effectively improve the thermoelectric properties, Energy Environ. Sci. 10 (2017) 799-807.
[43] J. Mao, J. Shuai, S. W. Song, Y. X. Wu, R. Dally, J. W. Zhou, Z. H. Liu, J. F. Sun, Q. Y. Zhang, C. Dela Cruz, S. Wilson, Y. Z. Pei, D. J. Singh, G. Chen, C. W. Chu, Z. F. Ren, Manipulation of ionized impurity scattering for achieving high thermoelectric performance in n-type Mg_3Sb_2-based materials, Proc. Natl. Acad. Sci. USA 114 (2017) 10548-10553.
[44] Z. H. Liu, N. Sato, W. H. Gao, K. Yubuta, N. Kawamoto, M. Mitome, K. Kurashima, Y. Owada, K. Nagase, C.-H. Lee, J. J. Yi, K. Tsuchiya, T. Mori, Demonstration of ultrahigh thermoelectric efficiency of ~7.3% in Mg_3Sb_2/MgAgSb module for low-temperature energy harvesting, Joule 5 (2021) 1196-1208.
[45] L. H. Huang, T. Liu, X. B. Mo, G. C. Yuan, R. Y. Wang, H. Liu, X. B. Lei, Q. Y. Zhang, Z. F. Ren, Thermoelectric performance improvement of p-type Mg_3Sb_2-based materials by Zn and Ag co-doping, Mater. Today Phys. 21 (2021) 100564-100569.
[46] J. K. Burdett, G. J. Miller, Fragment formalism in main-group solids: applications to AlB_2, $CaAl_2Si_2$, $BaAl_4$, and related materials, Chem. Mater. 2 (1990) 12-26.
[47] Y. L. Cui, X. L. Zhang, B. Duan, J. L. Li, H. J. Yang, H. T. Wang, P. Wen, T. Gao, Z. Fang, G. D. Li, Y. Li, P. C. Zhai, Band structure and thermoelectric properties of Al-doped $Mg_{3-x}Al_xSb_2$ compounds, J. Mater. Sci.: Mater. Electron. 30 (2019) 15206-15213.
[48] K. Imasato, S. D. Kang, S. Ohno, G. J. Snyder, Band engineering in Mg_3Sb_2 by alloying with Mg_3Bi_2 for enhanced thermoelectric performance, Mater. Horiz. 5 (2018) 59-64.
[49] H. J. Shang, Z. X. Liang, C. C. Xu, J. Mao, H. W. Gu, F. Z. Ding, Z. F. Ren, N-Type $Mg_3Sb_{2-x}Bi_x$ Alloys as Promising Thermoelectric Materials, Research 2020 (2020) 1219461.
[50] R. Shu, Z. J. Han, A. Elsukova, Y. B. Zhu, P. Qin, F. Jiang, J. Lu, P. O. Å. Persson, J. Palisaitis, A. le Febvrier, W. Q. Zhang, O. Cojocaru‐Mirédin, Y. Yu, P. Eklund, W. S. Liu, Solid‐State Janus Nanoprecipitation Enables Amorphous‐Like Heat Conduction in Crystalline Mg_3Sb_2‐based Thermoelectric Materials, Adv. Sci. (2022) 2202594.
[51] D. Chen, F. Jiang, L. Fang, Y.-B. Zhu, C.-C. Ye, W.-S. Liu, Machine learning assisted discovering of new M_2X_3-type thermoelectric materials, Rare Met. 41 (2022) 1543-1553.
[52] G. S. Pomrehn, A. Zevalkink, W. G. Zeier, A. Walle, G. J. Snyder, Defect‐Controlled Electronic Properties in AZn_2Sb_2 Zintl Phases, Angew. Chem. Int. Ed. Engl. 126 (2014) 3490-3494.
[53] K. Y. Li, X. T. Wang, F. F. Zhang, D. F. Xue, Electronegativity identification of novel superhard

materials, Phys. Rev. Lett. 100 (2008) 235504-235507.
[54] A. L. Allred, A Scale of Electronegativity based on Electronic Forces, J. Inorg. Nucl. Chem. 5 (1958) 264-268.
[55] Weast, RobertC, CRC Handbook of Chemistry and Physics, CRC Press, Florida, 1988.
[56] P. Gorai, B. R. Ortiz, E. S. Toberer, V. Stevanović, Investigation of n-type doping strategies for Mg_3Sb_2, J. Mater. Chem. A 6 (2018) 13806-13815.
[57] J. Li, S. Zhang, S. Zheng, Z. Zhang, B. Wang, L. Chen, G. Lu, Defect Chemistry for N-Type Doping of Mg_3Sb_2-Based Thermoelectric Materials, J. Phys. Chem. C 123 (2019) 20781-20788.
[58] A. Bhardwaj, D. K. Misra, Enhancing thermoelectric properties of a p-type Mg_3Sb_2-based Zintl phase compound by Pb substitution in the anionic framework, RSC Adv. 4 (2014) 34552-34560.
[59] Z. Ren, J. Shuai, J. Mao, Q. Zhu, S. Song, Y. Ni, S. Chen, Significantly enhanced thermoelectric properties of p-type Mg_3Sb_2 via co-doping of Na and Zn, Acta Mater. 143 (2018) 265-271.
[60] X. X. Chen, H. J. Wu, J. Cui, Y. Xiao, Y. Zhang, J. Q. He, Y. Chen, J. Cao, W. Cai, S. J. Pennycook, Z. H. Liu, L.-D. Zhao, J. H. Sui, Extraordinary thermoelectric performance in n-type manganese doped Mg_3Sb_2 Zintl: High band degeneracy, tuned carrier scattering mechanism and hierarchical microstructure, Nano Energy 52 (2018) 246-255.
[61] J. Li, F. Jia, S. Zhang, S. Q. Zheng, B. Y. Wang, L. Q. Chen, G. W. Lu, L. M. Wu, The manipulation of substitutional defects for realizing high thermoelectric performance in Mg_3Sb_2-based Zintl compounds, J. Mater. Chem. A 7 (2019) 19316-19323.
[62] L. R. Song, J. W. Zhang, B. B. Iversen, Thermal stability of p-type Ag-doped Mg_3Sb_2 thermoelectric materials investigated by powder X-ray diffraction, Phys. Chem. Chem. Phys. 21 (2019) 4295-4305.
[63] Y. Wang, X. Zhang, Y. Q. Liu, Y. Z. Wang, J. X. Zhang, M. Yue, Optimizing the thermoelectric performance of p-type Mg_3Sb_2 by Sn doping, Vacuum 177 (2020) 109388-109394.
[64] K. Imasato, S. Anand, R. Gurunathan, G. J. Snyder, The effect of Mg_3As_2 alloying on the thermoelectric properties of n-type $Mg_3(Sb, Bi)_2$, Dalton Trans. 50 (2021) 9376-9382.
[65] H. Shang, J. Zhang, H. Gu, S. Song, C. L. Chen, J. F. Lee, K. Shih, Z. F. Ren, F. Z. Ding, Depressed lattice oxygen and improved thermoelectric performance in N-type $Mg_3Bi_{2-x}Sb_x$ via La-doping, Mater. Today Phys. 21 (2021) 100485-100491.
[66] J. Ding, T. Lanigan-Atkins, M. Calderón-Cueva, A. Banerjee, D. L. Abernathy, A. Said, A. Zevalkink, O. Delaire, Soft anharmonic phonons and ultralow thermal conductivity in $Mg_3(Sb, Bi)_2$ thermoelectrics, Sci. Adv. 7 (2021) 1449-1455.
[67] J. Zhang, L. Song, B. B. Iversen, Improved Thermoelectric Properties of N-Type Mg_3Sb_2 through Cation-Site Doping with Gd or Ho, ACS Appl. Mater. Interfaces 13 (2021) 10964-10971.
[68] K. J. Liu, C. Chen, X. F. Li, J. C. Jia, C. L. Xia, J. Mao, Q. Huang, J. H. Sui, F. Cao, X. J. Liu, Y. Chen, Q. Zhang, Tuning the Carrier Scattering Mechanism by Rare-Earth Element Doping for High Average zT in Mg_3Sb_2-Based Compounds, ACS Appl. Mater. Interfaces 14 (2022) 7022-7029.
[69] W. Y. Zhu, W. Q. Fang, J. H. Zou, S. J. Zhu, J. X. Si, Enhanced Thermoelectric Performance of Indium-Doped n-type Mg_3Sb_2-Based Materials Synthesized by Rapid Induction Melting, J. Electron. Mater. 51 (2022) 1591-1596.
[70] X. Sun, X. Li, J. Yang, J. Xi, R. Nelson, C. Ertural, R. Dronskowski, W. Liu, G. J. Snyder, D. J. Singh, W. Zhang, Achieving band convergence by tuning the bonding ionicity in n-type Mg_3Sb_2, J. Comput. Chem. 40 (2019) 1693-1700.
[71] Z. J. Han, Z. G. Gui, Y. B. Zhu, P. Qin, B. P. Zhang, W. Q. Zhang, L. Huang, W. S. Liu, The Electronic Transport Channel Protection and Tuning in Real Space to Boost the Thermoelectric

Performance of $Mg_{3+\delta}Sb_{2-y}Bi_y$ near Room Temperature, Research 2020 (2020) 1672051.
[72] W. S. Liu, H. S. Kim, Q. Jie, Z. F. Ren, Importance of high power factor in thermoelectric materials for power generation application: A perspective, Scr. Mater. 111 (2016) 3-9.
[73] G. Rogl, A. Grytsiv, P. Rogl, E. Bauer, M. B. Kerber, M. Zehetbauer, S. Puchegger, Multifilled nanocrystalline p-type didymium – Skutterudites with ZT > 1.2, Intermetallics 18 (2010) 2435-2444.
[74] W.-S. Liu, Q. Y. Zhang, Y. C. Lan, S. Chen, X. Yan, Q. Zhang, H. Wang, D. Z. Wang, G. Chen, Z. F. Ren, Thermoelectric Property Studies on Cu-Doped n-type $Cu_xBi_2Te_{2.7}Se_{0.3}$ Nanocomposites, Adv. Energy Mater. 1 (2011) 577-587.
[75] J. Mao, H. T. Zhu, Z. W. Ding, Z. H. Liu, A. Gamage Geethal, G. Chen, Z. F. Ren, High thermoelectric cooling performance of n-type Mg_3Bi_2-based materials, Science 365 (2019) 495-498.
[76] F. Zhang, C. Chen, H. H. Yao, F. X. Bai, L. Yin, X. F. Li, S. Li, W. H. Xue, Y. M. Wang, F. Cao, X. J. Liu, J. H. Sui, Q. Zhang, High-Performance N-type Mg_3Sb_2 towards Thermoelectric Application near Room Temperature, Adv. Funct. Mater. 30 (2019) 1906143-1906149.
[77] X. L. Shi, J. Zou, Z. G. Chen, Advanced Thermoelectric Design: From Materials and Structures to Devices, Chem. Rev. 120 (2020) 7399-7515.
[78] M. Wood, J. J. Kuo, K. Imasato, G. J. Snyder, Improvement of Low-Temperature zT in a Mg_3Sb_2-Mg_3Bi_2 Solid Solution via Mg-Vapor Annealing, Adv. Mater. 31 (2019) 1902337.
[79] H. J. Shang, Z. X. Liang, C. C. Xu, S. W. Song, D. X. Huang, H. W. Gu, J. Mao, Z. F. Ren, F. Z. Ding, N-type $Mg_3Sb_{2-x}Bi_x$ with improved thermal stability for thermoelectric power generation, Acta Mater. 201 (2020) 572-579.
[80] Y.-K. Zhu, P. Wu, J. Guo, Y. Zhou, X. Chong, Z.-H. Ge, J. Feng, Achieving a fine balance in mechanical properties and thermoelectric performance in commercial Bi_2Te_3 materials, Ceram. Int. 46 (2020) 14994-15002.
[81] Y.-X. Zhang, Y.-K. Zhu, J. Feng, Z.-H. Ge, Precious metal nanoparticles dispersing toward highly enhanced mechanical and thermoelectric properties of copper sulfides, J. Alloys Compd. 892 (2022) 162035-162044.
[82] J. Li, S. Zhang, F. Jia, S. Q. Zheng, X. L. Shi, D. Q. Jiang, S. Y. Wang, G. W. Lu, L. M. Wu, Z.-G. Chen, Point defect engineering and machinability in n-type Mg_3Sb_2-based materials, Mater. Today Phys. 15 (2020) 100269-100277.
[83] L. Wang, J. Li, Y. Xie, L. Hu, F. Liu, W. Ao, J. Luo, C. Zhang, Tailoring the chemical bonding of GeTe-based alloys by MgB_2 alloying to simultaneously enhance their mechanical and thermoelectric performance, Mater. Today Phys. 16 (2021) 100308-100317.
[84] D. Y. Bao, J. Chen, Y. Yu, W. D. Liu, L. S. Huang, G. Han, J. Tang, D. L. Zhou, L. Yang, Z.-G. Chen, Texture-dependent thermoelectric properties of nano-structured Bi_2Te_3, Chem. Eng. J. 388 (2020) 124295-124302.
[85] K. Tyagi, B. Gahtori, S. Bathula, M. Jayasimhadri, S. Sharma, N. K. Singh, D. Haranath, A. K. Srivastava, A. Dhar, Crystal structure and mechanical properties of spark plasma sintered Cu_2Se: An efficient photovoltaic and thermoelectric material, Solid State Commun. 207 (2015) 21-25.
[86] J. F. Fu, X. L. Su, H. Y. Xie, Y. G. Yan, W. Liu, Y. H. You, X. Cheng, C. Uher, X. F. Tang, Understanding the combustion process for the synthesis of mechanically robust SnSe thermoelectrics, Nano Energy 44 (2018) 53-62.
[87] Z. H. Liu, W. H. Gao, X. F. Meng, X. B. Li, J. Mao, Y. M. Wang, J. Shuai, W. Cai, Z. F. Ren, J. H. Sui, Mechanical properties of nanostructured thermoelectric materials α-MgAgSb, Scr. Mater. 127 (2017) 72-75.

[88] A. Roy, P. Sreeramagiri, T. Babuska, B. Krick, P. K. Ray, G. Balasubramanian, Lattice distortion as an estimator of solid solution strengthening in high-entropy alloys, Mater. Charact. 172 (2021) 110877-110886.

Figures:

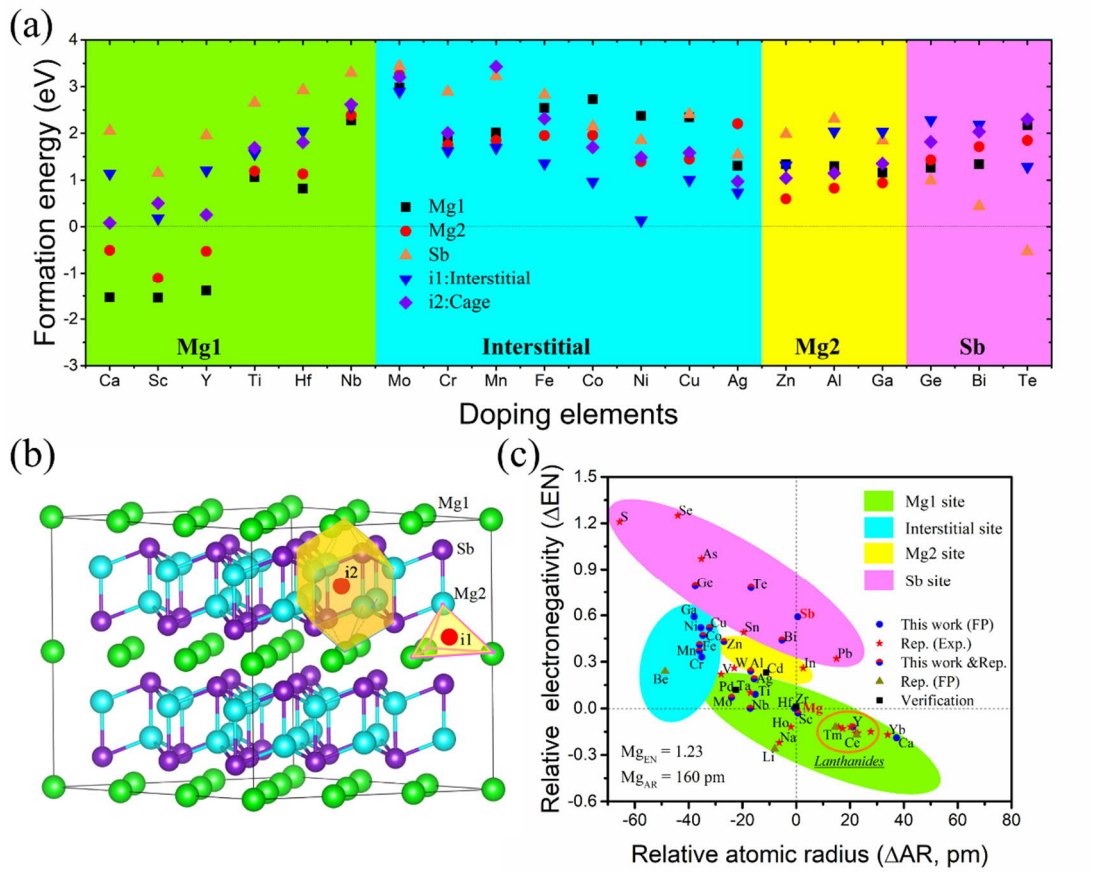

Fig. 1. (a) Defect formation energies of different doping sites of Mg_3Sb_2 material with extrinsic doped elements in their neutral state. (b) Crystal structure of Mg_3Sb_2 and their schematic doping site: Mg1, Mg2, Sb, interstitial (i1), and cage (i2). (c) Doping diagram for Mg_3Sb_2-based thermoelectric materials based on the difference of relative electronegativity and atomic radius of extrinsic dopants with Mg element. The blue circles represents for the elements has been theoretically calculated in this work. Red stars indicates the elements have been doped in Mg_3Sb_2-based materials. The circles in half blue and half red stands for the elements have been studied both in our work and in reported experiments. The elements in brown triangles are reported by theorectical calculations. Elements Cd and Pd are added for the verification of our doping diagram.

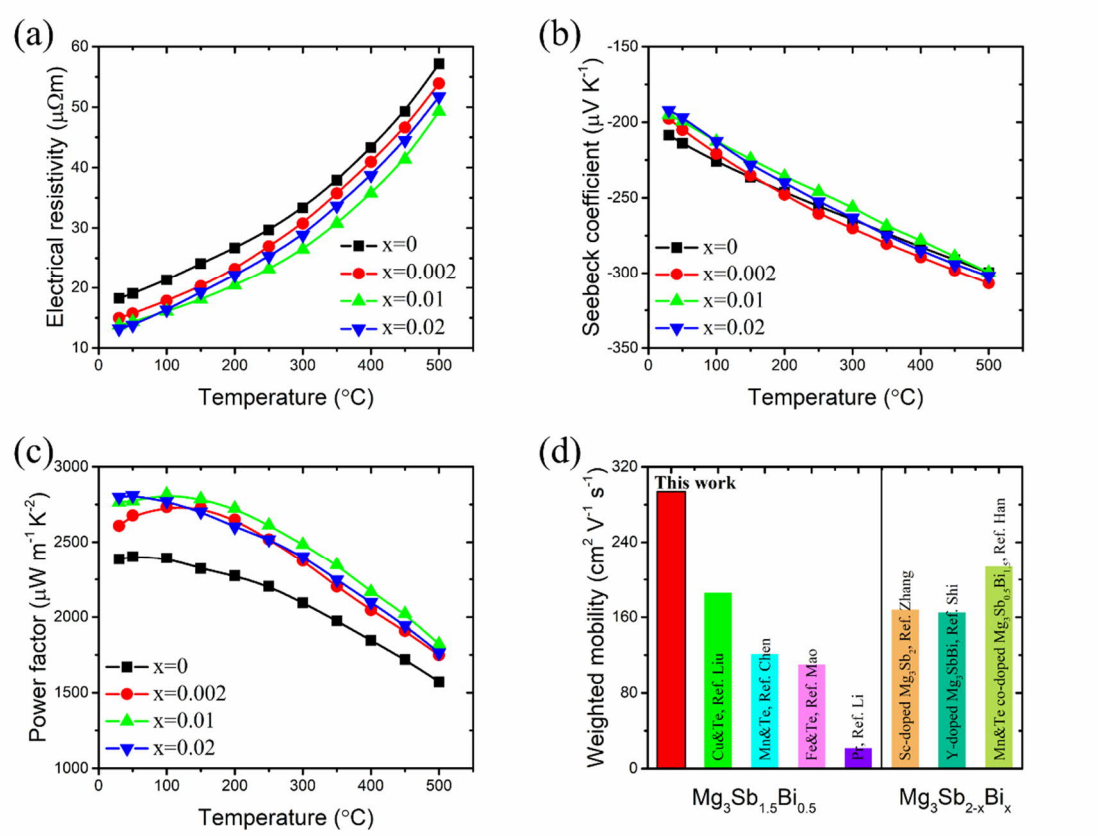

Fig. 2. Temperature independent electrical properties of the as-fabricated TM_x:$Mg_3Sb_{1.5}Bi_{0.5}$ bulks (x = 0, 0.002, 0.01, 0.02): (a) Electrical resistivity, (b) Seebeck coefficient, (c) power factor. (d) Weighted mobility of the as-fabricated $TM_{0.01}Mg_{3.2}Sb_{1.5}Bi_{0.5}$ sample and compared with other reported doped $Mg_3Sb_{2-x}Bi_x$ materials [26, 27, 43, 44, 60, 61, 71].

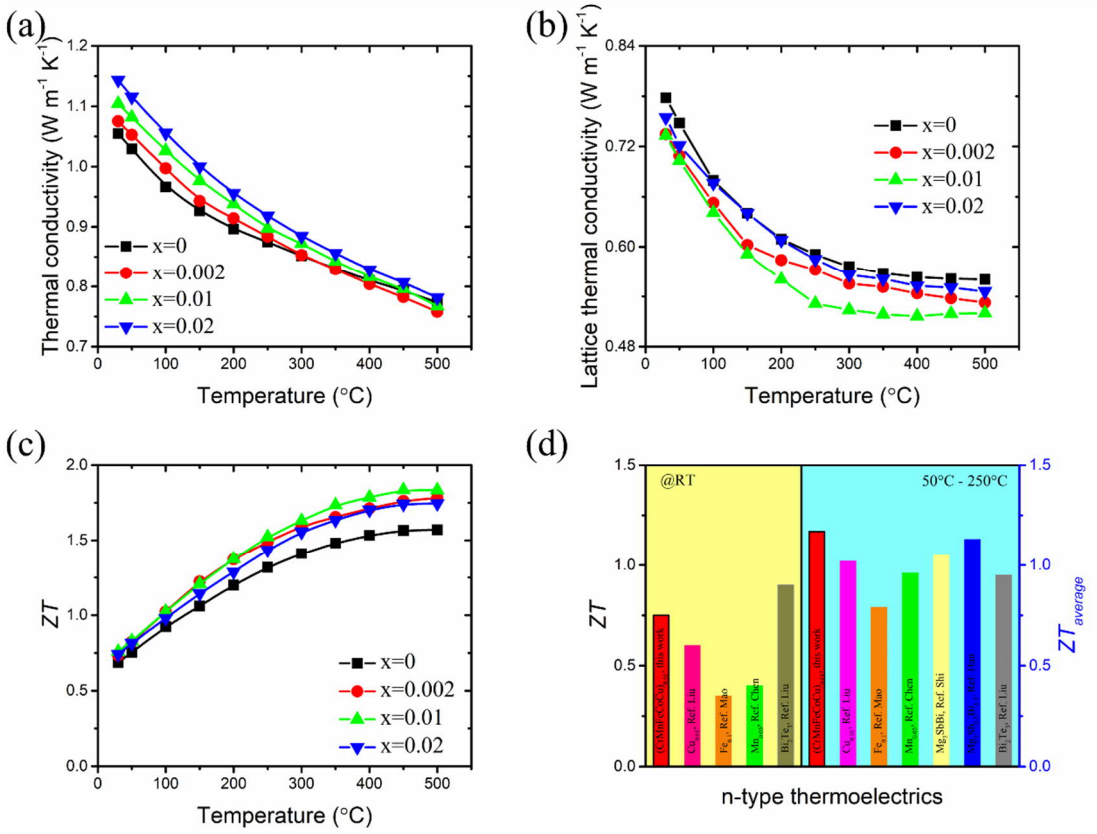

Fig. 3. Temperature dependent thermal properties of $TM_xMg_{3.2}Sb_{1.5}Bi_{0.49}Te_{0.01}$ (x = 0, 0.002, 0.01, 0.02): (a) Total thermal conductivity, (b) lattice thermal conductivity, and (c) dimensionless figure of merit ZT. (d) The comparison of ZT @RT and ZT_{avg} (50°C - 250°C) with other n-type Mg_3Sb_2-based thermoelectrics [26, 43, 44, 60, 71, 74].

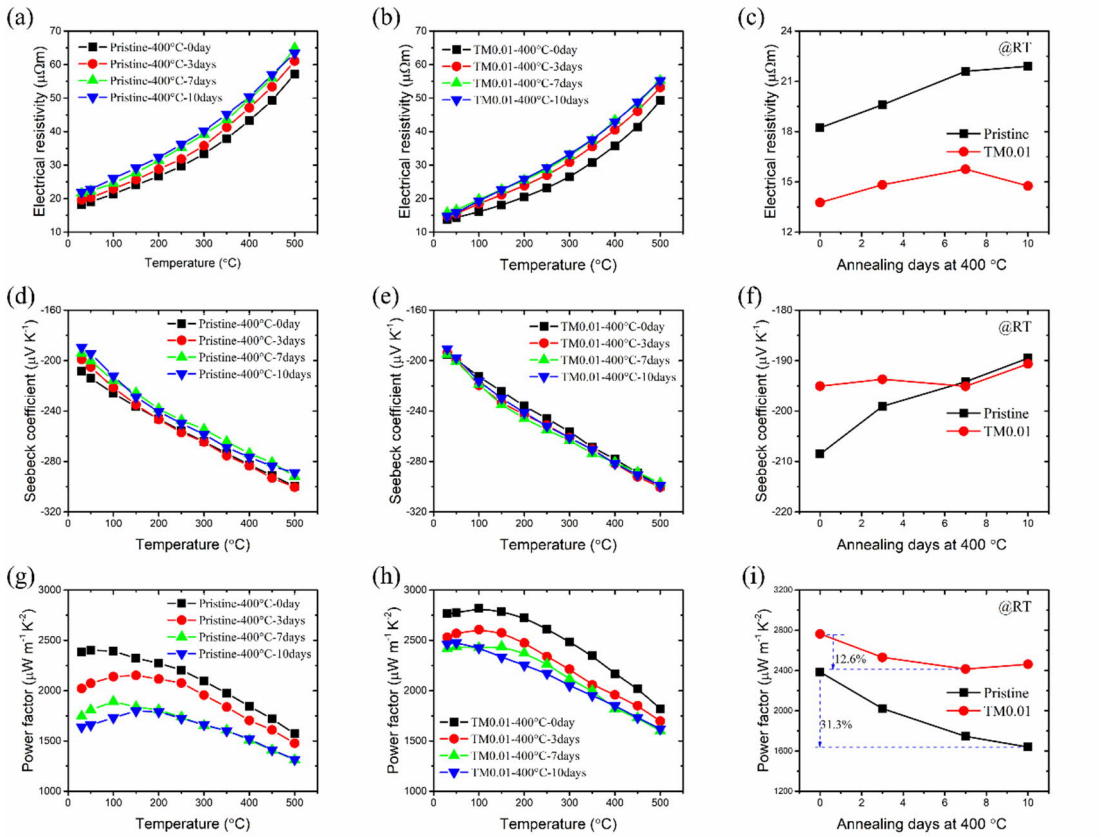

Fig. 4. Temperature independent electrical properties of pristine and $TM_{0.01}Mg_3Sb_{1.5}Bi_{0.5}$ system annealed at 400 °C for 0 day, 3 days, 7 days and 10 days and their comparison at room temperature: (a-c) electrical resistivity, (d-f) Seebeck coefficient, and (g-i) power factor.

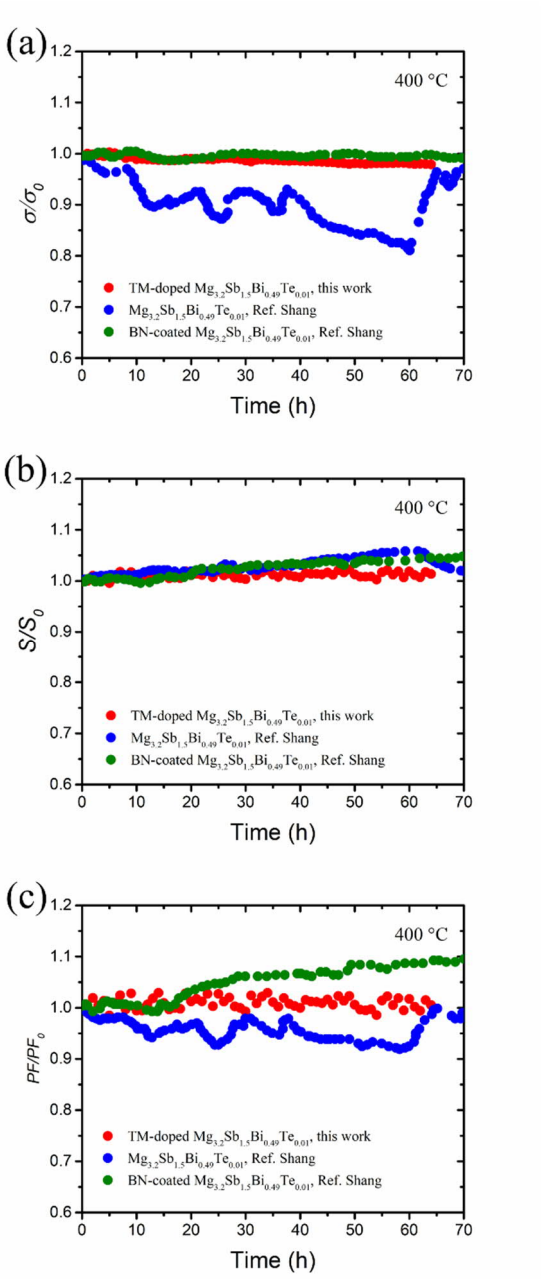

Fig. 5. Long-term in-situ measurement of electrical properties of the as-fabricated $TM_{0.01}Mg_3Sb_{1.5}Bi_{0.5}$ sample and compared with reported pristine and BN-coated $Mg_3Sb_{1.5}Bi_{0.5}$ [79] at 400 °C: (a) Electrical conductivity, (b) Seebeck coefficient, and (c) power factor.

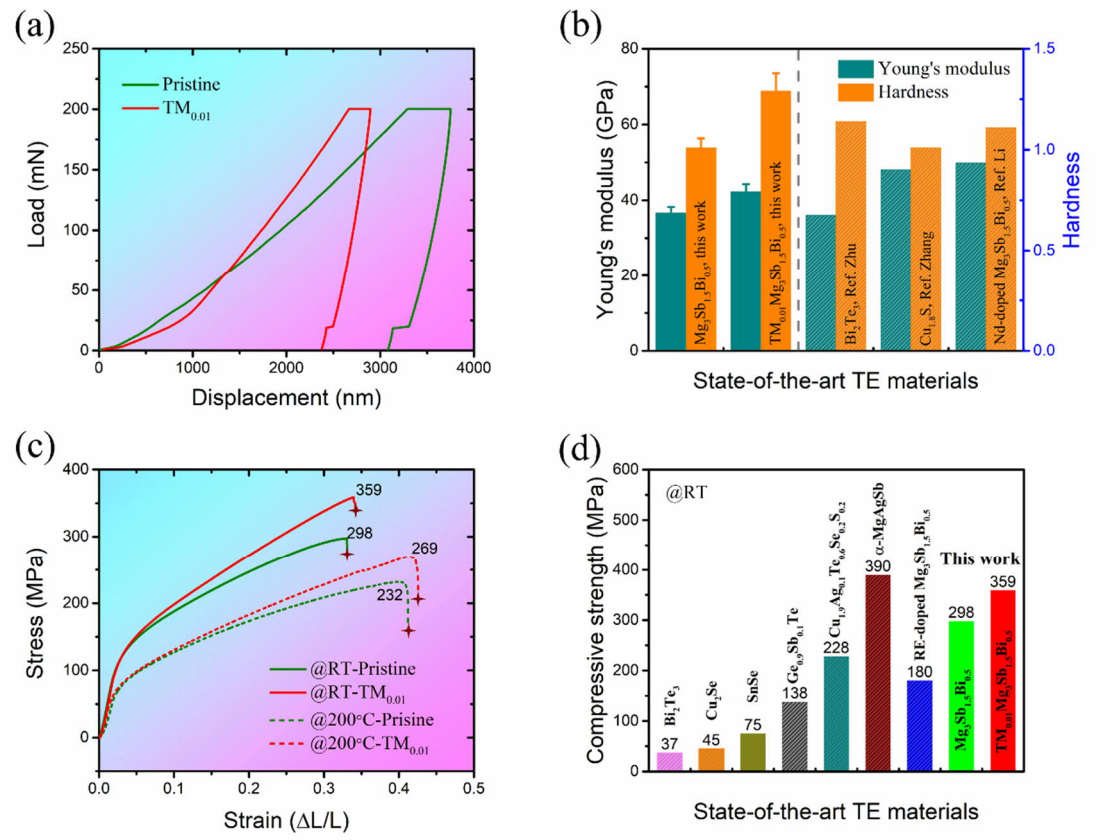

Fig. 6. Mechanical properties of pristine and $TM_{0.01}Mg_3Sb_{1.5}Bi_{0.5}$ materials. (a) Nanoindentation curves; (b) Young's modulus and Hardness as compared with reported thermoelectric materials [80-82]. (c) Compressive curves at room temperature and 200 °C. (d) Room temperature compressive strength of pristine and $TM_{0.01}Mg_3Sb_{1.5}Bi_{0.5}$ as compared with other start-of-the-art thermoelectric materials [13, 68, 83-87].

Tables:

Table 1 Room temperature Hall carrier concentration and carrier mobility of the as-fabricated TM_x:$Mg_3Sb_{1.5}Bi_{0.5}$ sample.

Sample	**n (10^{19} cm^{-3})**	**μ (cm^2 V^{-1} s^{-1})**
$Mg_{3.2}Sb_{1.5}Bi_{0.49}Te_{0.01}$	2.75	124.00
$TM_{0.002}Mg_{3.2}Sb_{1.5}Bi_{0.49}Te_{0.01}$	2.79	148.88
$TM_{0.01}Mg_{3.2}Sb_{1.5}Bi_{0.49}Te_{0.01}$	2.83	159.76
$TM_{0.02}Mg_{3.2}Sb_{1.5}Bi_{0.49}Te_{0.01}$	3.34	141.36